



CHORUS

This is the accepted manuscript made available via CHORUS. The article has been published as:

Detection of magnetic circular dichroism in amorphous materials utilizing a single-crystalline overlayer

J. Lin, X. Y. Zhong, C. Song, J. Ruzs, V. Kocevski, H. L. Xin, B. Cui, L. L. Han, R. Q. Lin, X. F. Chen, and J. Zhu

Phys. Rev. Materials **1**, 071404 — Published 27 December 2017

DOI: [10.1103/PhysRevMaterials.1.071404](https://doi.org/10.1103/PhysRevMaterials.1.071404)

Detection of magnetic circular dichroism in amorphous materials utilizing a single-crystalline overlayer

J. Lin¹, X.Y. Zhong^{1*}, C. Song², J. Ruzs³, V. Kocevski^{3,4}, H.L. Xin⁵, B. Cui², L.L. Han⁵, R.Q. Lin⁵, X.F. Chen¹, and J. Zhu¹

¹National Center for Electron Microscopy in Beijing, Key Laboratory of Advanced Materials (MOE), State Key Laboratory of New Ceramics and Fine Processing, School of Materials Science and Engineering, Tsinghua University, Beijing 100084, China.

²Key Laboratory of Advanced Materials (MOE), School of Materials Science and Engineering, Tsinghua University, Beijing 100084, China.

³Department of Physics and Astronomy, Uppsala University, Box 516, Uppsala S-75120, Sweden.

⁴Department of Materials Science and Engineering, Northwestern University, Evanston, Illinois 60208, USA.

⁵Center for Functional Nanomaterials, Brookhaven National Laboratory, Upton, New York 11973, USA.

*e-mail: xyzhong@mail.tsinghua.edu.cn

Electron energy-loss magnetic chiral dichroism (EMCD) is a novel technique that allows the magnetic information determination down to the nanoscale. However, constrained by the predefined diffraction geometry in regular EMCD experiments, it has not yet been feasible to obtain EMCD signals from amorphous materials, due to the lack of long range ordering. Here we propose a protocol for EMCD detection in amorphous materials utilizing a single-crystalline overlayer acting as a two-beam splitter. Phase locking of the EMCD signals are observed and explained by two conceivable scenarios. Both experimental results and theoretical calculations demonstrate significant EMCD signals of amorphous materials.

With the development of nanostructured magnetic materials and devices, the detection of magnetic information on the nanometer scale has increasingly become a major challenge. Based on the desired diffraction geometry in single-crystalline materials, electron energy-loss magnetic chiral dichroism (EMCD) technique was first proposed in 2003 [1] and experimentally performed in 2006 [2]. Profiting from experimental and theoretical progresses these years, improvements on spatial resolution [3-5], theoretical calculation [6-12] and quantitative analysis [13-15] of spin and orbital magnetic moments have been achieved. Our previous work experimentally revealed that atomic site-specific magnetic structure information can be quantitatively determined on the nanometer scale using EMCD technique [16-18]. In principle, only in single-crystalline form can the EMCD signals be acquired because specific scattering geometry, namely the two-beam [2,8,13,19,20] and three-beam [3,14,16,21] conditions, is essential in experimental EMCD setups. Recently Muto *et al.* demonstrated that EMCD signals of a polycrystalline iron sample could also be extracted in a statistical method [22]. Since there are a great number of magnetic materials in practical applications

are non-crystalline such as the magnetic tunnel junctions and sensors, it requires us to pursue a better understanding of magnetic states and behaviors of non-crystalline materials. In our work, by devising an ingenious sample system, we represent the measurement of EMCD signals from an amorphous sample breaking through the aforementioned restriction of crystalline materials.

Fig. 1 shows the schematic diagram of our experimental setup. The magnetic amorphous thin film on a nonmagnetic single-crystal substrate is designed for detecting EMCD signals of amorphous materials. The crystalline layer oriented in two-beam condition serves as a beam splitter in the electron beam path. After passing through the crystalline overlayer, the incident electron beam is mainly separated into one transmitted beam and one diffracted beam, exerted a phase shift due to dynamical diffraction effects [23]. These two beams can interact with magnetic atoms in the amorphous layer both inelastically and elastically. The possibility of elastically scattered electrons in the amorphous materials with a few nanometers thickness is relatively low, indicating that the transmitted and diffracted beams remain almost undistorted. The EMCD signals of the amorphous layer can be determined by the difference between the two normalized spectra taken at the positions ‘+’ and ‘-’ known as Thales positions under two-beam condition of the single-crystalline overlayer.

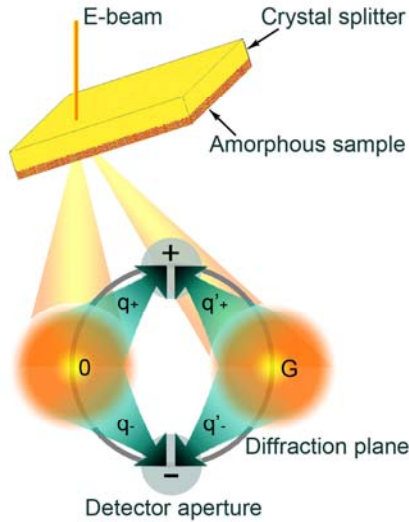


FIG. 1. Schematics of the measurement proposed for EMCD spectroscopy of amorphous materials. The bilayer sample with a magnetic amorphous layer (red) growing on a single-crystalline substrate (yellow) is tilted to the substrate’s two-beam condition in the illustration of parallel electron beam. The large circle on diffraction plane is indicative of that the momentum transfer \mathbf{q} is perpendicular to. The detector apertures are placed at the Thales positions labeled by ‘+’ and ‘-’ in the gray small circles.

Here, we fabricated the FeO_x amorphous thin film on an Yttrium-stabilized ZrO_2 (YSZ) (111) single-crystalline substrate using the magnetron sputtering method at room temperature. Fig. 2(a) shows the typical X-ray photoelectron spectroscopy (XPS) result of Fe 2p core spectrum from the FeO_x thin film, indicating that the Fe is present in forms of Fe^{2+} and Fe^{3+} within the FeO_x layer. In Fig. 2(b), the scanning transmission electron microscopy (STEM) - electron energy-loss spectroscopy (EELS) mapping carried out on a JEOL 2100F shows the cross-sectional elemental distribution of Fe and O, which also confirms that the thin films continuously grown on the YSZ substrate are composed of FeO_x . The high-resolution Z-contrast image in Fig. 2(c) taken on an aberration-corrected Hitachi HD-2700C operated at 200 kV clearly reveals the disordered structure

in the amorphous FeO_x layer without regular crystallographic fringes and the atomic-scale lattice image in the single-crystalline YSZ substrate. There is not any diffraction reflection in the Fourier transform pattern of the FeO_x area in the inset, experimentally confirming that the crystal structure of the FeO_x layer is amorphous. Combining with the high-resolution scanning electron microscope image of the FeO_x layer (see supplementary Fig. S1), the thickness of the amorphous layer is approximately estimated to be from 2 nm to 5 nm. The transmission electron microscope (TEM) image and selected area electron diffraction pattern of the plane-view sample along the [111] zone axis of the YSZ substrate are displayed in Fig. 2(d). The EMCD experiments were carried out in the sample area marked by the white dotted circle, of which the thickness is around 30 nm.

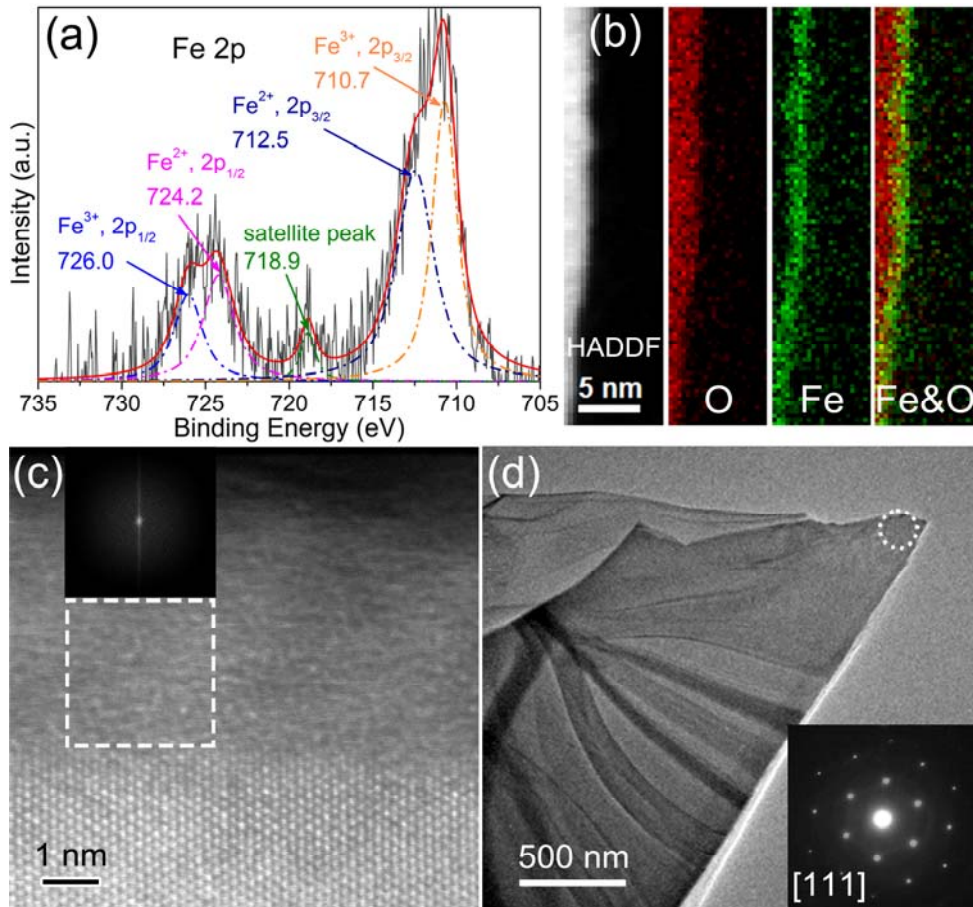


FIG. 2. Composition and structure characterizations of FeO_x/YSZ . (a) Typical XPS measurement of Fe 2p core spectrum for FeO_x layer. The peaks at 710.7 and 712.5 eV are attributed to the binding energies of the $2p_{3/2}$ orbital of Fe^{2+} and Fe^{3+} species, respectively. For the $2p_{1/2}$ band, the peak at 724.2 eV is assigned to the binding energy of Fe^{2+} , and the peak for Fe^{3+} appears at 726.0 eV. The peak at 718.9 eV is a satellite peak. This result indicates the oxide layer consists of Fe^{2+} and Fe^{3+} , which can be written as FeO_x . (b) STEM-EELS mapping of FeO_x/YSZ shows the elemental distribution of Fe and O. The red distribution refers to O and the green refers to Fe. The red part occupies a wider area because YSZ contains O as well. (c) High-resolution cross-sectional STEM image of FeO_x/YSZ and the inset for Fourier transform of the FeO_x layer within the white dotted frame, which experimentally confirms that the crystal structure of the FeO_x layer is amorphous. (d) TEM image of the FeO_x/YSZ sample. The thickness of the detected area inside the white dotted circle is estimated to be 30 nm. The inset of the selected area electron diffraction pattern shows that the YSZ crystal nanopillars are along the [111] zone axis.

The magnetic-hysteresis loop measured by a superconducting quantum interference device shows that the entire FeO_x film exhibits soft ferromagnetic behaviors with a small coercive force of around 20 Oe (see Supplementary Fig. S2). The EMCD experiments were performed using a FEI Titan 80-300 TEM equipped with a post-column Gatan Tridium system, operated at 300 kV with an energy resolution of about 0.8 eV. Owing to the magnetic field of around 20000 Oe which is perpendicular to the specimen inside the TEM, the magnetization of the plane-view sample is saturated along the z-axis. According to our experimental design, the single-crystalline YSZ overlayer is tilted into the two-beam condition with (2 $\bar{2}$ 0) systematic reflections excited as shown in the left inset of experimental two-beam diffraction in Fig. 3(b). The EMCD spectra are acquired at the “+” and “-” positions of the Thales circle, which encloses the transmitted spot and the excited (2 $\bar{2}$ 0) diffraction spot. As a result of averaging 5 different spectra, Fig. 3(a) shows the significant EMCD signal strength of about 5% at Fe-L₃ edge and a weak but detectable EMCD signal at Fe-L₂ edge of the amorphous FeO_x layer.

In order to confirm that the experimental dichroic signals are magnetic, the external magnetic field switched from 2 T under the standard TEM mode to -0.4 T under the Lorentz mode. In the Lorentz mode, the out-of-plane external magnetic field perpendicular to the sample varied from -0.4 T to 2.3 T by changing the excitation current of objective lens. According to the small coercive force of about 20 Oe in the magnetic hysteresis loop of amorphous FeOx thin films, the net magnetic moments of FeOx follow the external magnetic field. When the external field is set to -0.4 T, the reversal of magnetic moments of Fe atoms are evident since an opposite difference emerges from “+” and “-” EEL Spectra as shown in the inset of Fig. 3(a).

After the extraction of EMCD signals, we also performed the X-ray magnetic circular dichroism (XMCD) measurement on a FeO_x/YSZ sample, in which the amorphous FeO_x layer grown under the same condition was about 10 nm in this case. The XMCD measurements were carried out in total electron yield mode at the Beamline BL08U1A in Shanghai Synchrotron Radiation Facility at 300 K. The measured XMCD spectrum shown in Fig. 3(b) is similar to the EMCD results, especially in terms of signal strength and signal sign. Since the interaction depth of XMCD is routinely 6 nm, we conclude that the XMCD signal of Fe originates from within the FeO_x layer only.

Furthermore, we apply the sum rules to the signals of EMCD and XMCD to calculate the orbital/spin moment ratio (m_L/m_S ratio), which is given by the following equation[7,8]

$$\frac{m_L}{m_S} = \frac{2 \int_{L_3} \Delta\sigma(E)dE + \int_{L_2} \Delta\sigma(E)dE}{3 \int_{L_3} \Delta\sigma(E)dE - 2 \int_{L_2} \Delta\sigma(E)dE} = \frac{2q}{9p - 6q} \quad (1)$$

where q , p are the energy integrals of the MCD spectrum over both edges and the L₃ edge only, respectively. As is pointed in Fig. 3, $p = 1$ and $q = 0.12$ after the normalization in the case of the EMCD spectrum, while $p' = 1$ and $q' = 0.08$ after the normalization in the case of the XMCD spectrum. We calculate $m_L/m_S = 0.03 \pm 0.02$ from the EMCD spectra, while we obtain $m_L/m_S = 0.02$ from the XMCD spectra. Considering of the error from the noise in spectra, the quantitative magnetic parameter extracted from experimental EMCD spectra is quite similar to that from experimental XMCD spectra. Note that the random noise seen in the EMCD spectra is partially averaged out thanks to the integration over wider energy ranges, as indicated in the Eq. (1) and the error of the m_L/m_S value mostly originates from post-edge normalization and fluctuations of the cumulative sum in that energy range, see the green curve in Fig.3(a).

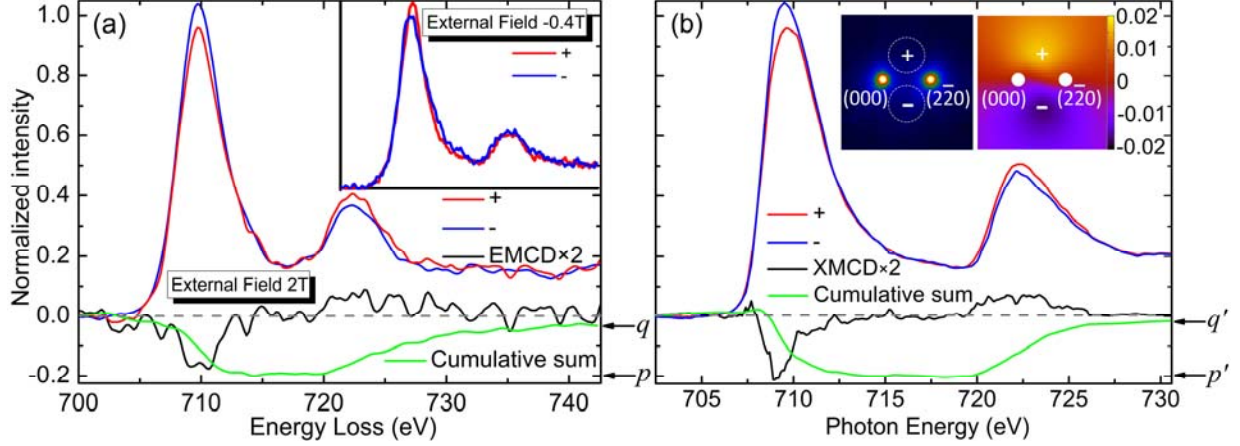


FIG. 3. EMCD and XMCD spectra. (a) Measured Fe- $L_{2,3}$ edges for FeO_x/YSZ in the two configurations from '+' and '-' (shown in red and blue, respectively), as well as the EMCD signal (the difference spectrum magnified by a factor of 2, shown in black) under 2 T in the TEM mode. The inset shows the reversal of the EMCD signal under -0.4 T in the Lorentz mode. (b) The Fe- $L_{2,3}$ edges in the two configurations from '+' and '-' (shown in red and blue, respectively), as well as the XMCD signal (the difference spectrum magnified by a factor of 2, shown in black). The insets of diffraction plane show the experimental two-beam symmetrical excited diffraction spots (false color, left) and an example simulation of the relative EMCD strength (right), respectively.

In order to understand this physical process from the theoretical point of view, we carry out the calculations following the formalism for a combined multislice/Bloch-waves method [24]. For an amorphous material, we can write the following expression for the double-differential scattering cross-section

$$\frac{\partial^2 \sigma}{\partial E \partial \Omega} = \sum_a \sum_{gg'} F_{g_x, g_y}^{(a_z)} F_{g'_x, g'_y}^{(a_z)*} e^{i(q-q') \cdot a} \frac{S_a(q, q', E)}{q^2 q'^2} \quad (1)$$

where $F_{g_x, g_y}^{(a_z)}$ is the (g_x, g_y) -component of z -dependent Fourier transformed probe wave function and

$S_a(q, q', E)$ is the mixed dynamical form factor (MDFF) [25] from a single atom at position \mathbf{a} with momentum transfer vectors \mathbf{q} and \mathbf{q}' and energy loss E . Focusing on EMCD only, we are interested in the imaginary part of MDFFs. Assuming that magnetic moment is along z -direction, in two-beam case we obtain

$$\text{EMCD}_{1,2} \propto \frac{4M_z}{G^2} \sum_a \text{Im} \left[F_{\frac{G}{2}, 0}^{(a_z)} F_{\frac{G}{2}, 0}^{(a_z)*} e^{iG a_z} \right] \quad (2)$$

where we have silently assumed that the M_z is approximately the same for all atoms and summed over all magnetic atoms with coordinates $\mathbf{a} = (a_x, a_y, a_z)$.

The structure models prepared by molecular dynamics simulations represent an ideally amorphous structure. High annealing temperature guaranteed a strong random movement of atoms, destroying any sort of crystallinity. The subsequent cooling times in molecular dynamics simulations are, with today available computational resources, necessarily by several orders of magnitude faster than cooling in experiments, and in consequence, the structure model does not have enough of time to

establish the more realistic situation, where a medium range order appears. Moreover, our molecular dynamics simulations do not include the substrate. Therefore the surface of our structure model does not reflect the periodicity of the substrate. This is again in contrast to experiment, where during a gradual growth of the thin layer of magnetic oxide, it is likely that the first deposited atoms will occupy some energetically favorable positions on the YSZ surface plane. Such positions repeat periodically, as dictated by crystal structure of YSZ.

In consequence, the strength of $\sim 4\%$ in the particular simulation of EMCD signal shown in the right inset of Fig. 3(a) is lower than the observed one of $\sim 5\%$ (in details, see Supplementary Fig. S3). Moreover, according to theoretical calculations, the sign of the predicted EMCD signal sensitively depends on the beam position in our simulations—and this is in disagreement with experiments. Particularly the latter aspect suggests that some sort of phase-locking mechanism must be in action in the experiments, which forces a non-negligible fraction of the atoms in the oxide layer to occupy a certain discrete set of positions, dictated by the substrate. Otherwise a suitable net shift of all atoms with respect to the YSZ substrate can change sign of EMCD, alter its size or even completely cancel it out.

There are two conceivable phase locking scenarios. First, the first few monolayers of deposited iron oxide might occupy energetically favorable positions on the substrate, adopting its periodicity. This scenario is very likely to happen in a gradual growth of the iron oxide and that could provide such phase locking mechanism for the locally crystalline grains of the iron oxide, for which the initial few partially epitaxial monolayers would serve as seeds for growth of such grains. Second, even in an amorphous material, there is always a certain degree of medium range order, as is well known from medium range probes such as fluctuation electron microscopy [26,27]. It is well possible that both two scenarios are active to some degree. Medium range order is always present and can reach up to 1-3 nm. By itself it would not fix the sign of the EMCD signal, though. Imagine a randomly oriented crystalline grain of iron oxide somewhere within the layer. If its relative position with respect to the substrate is arbitrary, it would lead to random sign of the EMCD signal. Therefore, if the medium range order is actively contributing to the observed EMCD signal, then majority of such grains must have their positions restricted to a discrete set of placements and orientations with respect to the YSZ substrate.

Experimentally, it is very difficult to assess the particular phase locking scenario, which is in action in our samples. Studies of medium range order would require application of the fluctuation electron microscopy method, which goes well beyond our initial study of EMCD on amorphous materials. Likewise, assessing the preferential positions of the Fe ions within the first few layers of deposited iron oxide is very complicated. Thus we leave the question of the exact phase locking scenario in our sample unanswered, hoping to stimulate further research in this area. Simultaneously, we postulate that in a sufficiently thin layer of an amorphous material, grown on a crystalline substrate, there will be a tendency to such phase locking mechanism, providing means to detect EMCD signal in non-crystalline materials.

Indirectly, however, we point out the similarity between the XMCD and EMCD spectra from the two experiments. This a posteriori provides arguments that the oxide layer starts its growth with partially epitaxial relation to the substrate and via medium range order the oxide structure remains phase-locked to the substrate to a sufficient degree to show sizable EMCD. Yet, the structure is sufficiently amorphous, at least for a macroscopic probe, where no deviation from amorphousness has been detected. Thus we suggest that the measured EMCD spectra well represent the chemical

and magnetic situation in a bulk amorphous oxide.

In view of our experimental configurations, it extends the capabilities of EMCD technique to obtain the magnetic information of amorphous materials at the nanometer scale. It is well known that grain boundaries in magnetic materials play a different role on magnetic behaviors. However, it is quite challenging to access the magnetic information of grain boundaries with disordered structure at high spatial resolution. Our approach might provide the opportunity to distinguish the magnetic information at grain boundaries from that of grains. This method can be also applied to extract the magnetic information from the different phases in the heterogeneous amorphous materials at the nanometer scale.

In summary, our experimental setup opens the door for achieving nanoscale magnetic investigation of amorphous materials using EMCD. The approach allows us to break through the restriction of single-crystalline samples in regular EMCD signal measurements, providing new prospects of detecting EMCD spectra from amorphous materials. Consequently, it may pave a new era to apply EMCD techniques in the field of nanomagnetism as a unique characterization tool.

References

1. C. Hébert and P. Schattschneider, *Ultramicroscopy* **96**, 463-468 (2003).
2. P. Schattschneider, S. Rubino, C. Hébert, J. Ruzs, J. Kuneš, P. Novák, E. Carlino, M. Fabrizioli, G. Panaccione, and G. Rossi, *Nature* **441**, 486-488 (2006).
3. P. Schattschneider, M. Stöger-Pollach, S. Rubino, M. Sperl, C. Hurm, J. Zweck, and J. Ruzs, *Phys. Rev. B* **78**, 104413 (2008).
4. L. Jin, C. L. Jia, I. Lindfors-Vrejoiu, X. Y. Zhong, H. C. Du, and R. E. Dunin-Borkowski, *Adv. Mater. Interfaces*. **3**, 1600414 (2016).
5. D. S. Song, L. Ma, S. M. Zhou, and J. Zhu, *J. Appl. Phys.* **107**, 042401 (2015).
6. J. Ruzs, S. Rubino, and P. Schattschneider, *Phys. Rev. B* **75**, 214425 (2007).
7. J. Ruzs, O. Eriksson, P. Novák, and P. M. Oppeneer, *Phys. Rev. B* **76**, 060408(R) (2007).
8. L. Calmels, F. Houdellier, B. Warot-Fonrose, C. Gatel, M. J. Hÿtch, V. Serin, E. Snoeck, and P. Schattschneider, *Phys. Rev. B* **76**, 060409(R) (2007).
9. L. Calmels and J. Ruzs, *Ultramicroscopy* **110**, 1042-1045 (2010).
10. L. Calmels and J. Ruzs, *J. Appl. Phys.* **109**, 07D328 (2011).
11. S. Rubino, P. Schattschneider, J. Ruzs, J. Verbeeck, and K. Leifer, *J. Phys. D: Appl. Phys.* **43**, 474005 (2010).
12. J. Ruzs, S. Rubino, O. Eriksson, P. M. Oppeneer, and K. Leifer, *Phys. Rev. B* **84**, 064444 (2011).
13. H. Lidbaum, J. Ruzs, A. Liebig, B. Hjörvarsson, P. M. Oppeneer, E. Coronel, O. Eriksson, and K. Leifer, *Phys. Rev. Lett.* **102**, 037201 (2009).
14. B. Warot-Fonrose, C. Gatel, L. Calmels, V. Serin, and P. Schattschneider, *Ultramicroscopy* **110**, 1033-1037 (2010).
15. J. Ruzs, H. Lidbaum, S. Rubino, B. Hjörvarsson, P. M. Oppeneer, O. Eriksson, and K. Leifer, *Phys. Rev. B* **83**, 132402 (2011).
16. Z. Q. Wang, X. Y. Zhong, R. Yu, Z. Y. Cheng, and J. Zhu, *Nat. Commun.* **4**, 1395 (2013).
17. D. S. Song, J. Ruzs, J. W. Cai, and J. Zhu, *Ultramicroscopy* **169**, 44-54 (2016).
18. Z. C. Wang, X. Y. Zhong, L. Jin, X. F. Chen, Y. Moritomo, and J. Mayer, *Ultramicroscopy*, **176**, 212-217 (2017).
19. B. Warot-Fonrose, F. Houdellier, M. J. Hÿtch, L. Calmels, V. Serin, and E. Snoeck,

- Ultramicroscopy **108**, 393-398 (2008).
20. Z. H. Zhang, X. F. Wang, J. B. Xu, S. Muller, C. Ronning, and Q. Li, *Nat. Nanotech.* **4**, 523-527 (2009).
 21. M. Stöger-Pollach, C. D. Treiber, G. P. Resch, D. A. Keays, and I. Ennen, *Micron* **42**, 456-460 (2011).
 22. S. Muto, J. Ruzs, K. Tatsumi, R. Adam, S. Arai, V. Kocevski, P. M. Oppeneer, D. E. Bürgler, and C. M. Schneider. *Nat. Commun.* **5**, 3138 (2014).
 23. A. Howie and M. J. Whelan, *Proc. Roy. Soc.* **A263**, 217-237 (1961).
 24. J. Ruzs, S. Bhowmick, M. Eriksson, and N. Karlsson, *Phys.Rev.B* **89**, 134428 (2014).
 25. H. Kohl and H. Rose, *Adv. Electronics Electron Physics* **65**, 173-227(1985).
 26. M. M. J. Treacy and J. M. Gibson, *Acta Cryst.* **52**, 212-220 (1996).
 27. M. M. J. Treacy, J. M. Gibson, L. Fan, D. J. Paterson, and I. McNulty, *Rep. Prog. Phys.* **68**, 2899-2944 (2005).

Acknowledgements

This work was financially supported by National Key Research and Development Program (2016YFB0700402), National Natural Science Foundation of China (51671112, 51471096, 11374174, 51390471, 51527803, 51525102, 51390475, 51371031, 51571021), National Basic Research Program of China (2015CB921700, 2015CB654902), National Key Scientific Instruments and Equipment Development Project (2013YQ120353) and Tsinghua University (20141081200). This work made use of the resources of the National Center for Electron Microscopy in Beijing. We acknowledge Beamline BL08U1A in Shanghai Synchrotron Radiation Facility for XMCD measurements. We acknowledge Dr. D. Pohl and Dr. B. Rellinghaus at IFW Dresden, Institute for Metallic Materials for their aids in Lorentz experiments. J. Ruzs acknowledges financial support of Swedish Research Council, STINT and Göran Gustafsson's Foundation. H.L. Xin acknowledges support from the Center for Functional Nanomaterials, which is a U.S. DOE Office of Science Facility, at Brookhaven National Laboratory under Contract No. DE-SC0012704. We are grateful to Profs R. Yu, Dr. Y. Shao, Mrs. Z.Y. Cheng, Mr. D.S. Song for beneficial discussions, and Profs P. Yu, Dr. Z.P. Li and Mr. Z.Y. Liao for providing the substrate and preparing the specimen.